

Cosmological constraints from neighbor-density-weighted marked correlation functions

Xu Xiao,¹ Xiao-Dong Li,^{1,2,3,*} Yiqi Huang,^{1,†} and Le Zhang^{1,2,3,‡}

¹*School of Physics and Astronomy, Sun Yat-Sen University, Zhuhai 519082, China*

²*Peng Cheng Laboratory, Shenzhen, Guangdong 518066, China*

³*CSST Science Center for the Guangdong–Hong Kong–Macau Greater Bay Area, SYSU, Zhuhai 519082, China*

(Dated: May 25, 2026)

We investigate whether neighbor-density-weighted marked correlation functions (MCFs) can extract cosmological information beyond the standard redshift-space two-point correlation function (2PCF). Using the Kun suite of 129 $w_0w_a\text{CDM} + \sum m_\nu$ simulations in $1 h^{-1}\text{Gpc}$ boxes, we construct Gaussian-process emulators for the normalized scale statistic $\widehat{W}^\alpha(s)$ and the angular statistic $\widehat{W}_{\Delta s}^\alpha(\mu)$. We perform joint analyses combining multiple mark parameters α and quantify the information gain using the FoM in the $\Omega_m-\sigma_8$ plane. Relative to the 2PCF case, three-mark combinations improve the FoM by factors of 1.7–2.5, while five-mark combinations increase the gain to 1.9–2.4, depending on the statistic and mark definition. We further compare density and normalized-gradient marks, finding that they are nearly redundant for isotropic statistics but complementary for angular statistics, where their combination improves the FoM by up to 43%. Tests of scale range and halo selection show that the marked statistics remain robust under changes in analysis choices, with the angular statistic retaining additional cosmological information that is less sensitive to tracer selection. Our results demonstrate that MCFs substantially enhance cosmological constraints beyond the standard 2PCF and provide a robust probe for next-generation galaxy surveys.

PACS numbers:

I. INTRODUCTION

Modern galaxy surveys have established large-scale structure (LSS) as one of the most powerful and precise probes of cosmic expansion and structure growth. In particular, Stage-III surveys such as 2dFGRS, WiggleZ, and SDSS have firmly established two-point clustering statistics as a standard cosmological tool [1–9]. The two-point correlation function (2PCF) and its Fourier counterpart, the power spectrum, are widely used because of their simplicity, clear physical interpretation, and sensitivity to both the expansion history and the growth of structure [10–14]. These statistics have been successfully applied to a range of surveys, including 2dFGRS, 6dFGS, WiggleZ, and SDSS, yielding robust cosmological constraints [6–9, 15–27].

Looking ahead, ongoing and upcoming surveys such as DESI¹, LSST², Euclid³, Roman⁴, and CSST⁵ will map substantially larger cosmic volumes with higher tracer densities [28–33]. These Stage-IV surveys will substantially improve statistical precision, increasing the need for summary statistics that can fully exploit the available information. However, the limitations of standard two-point statistics are well recognized. Nonlinear gravitational evolution, galaxy bias, and redshift-space distortions induce non-Gaussian features in the density field that cannot be fully captured by an unweighted

two-point statistic. As a result, part of the cosmological information is inevitably lost when compressing the data into the 2PCF or power spectrum alone.

This limitation has motivated the development of alternative approaches that go beyond the Gaussian two-point level, including higher-order correlation functions, void statistics, and machine-learning-based summaries [34–41]. These methods aim to retain the robustness and interpretability of traditional statistics while capturing additional non-Gaussian information present in LSS. Among these, marked correlation functions (MCFs) provide a particularly simple and flexible extension of the standard two-point framework [42–52]. In this approach, each tracer is assigned a mark that depends on its local environment, and clustering is quantified through a weighted two-point statistic. The standard 2PCF is recovered when all marks are unity. By construction, MCFs probe the environmental dependence of clustering, allowing one to emphasize overdense or underdense regions through appropriate choices of the mark. Previous studies using mock catalogs and SDSS data have demonstrated that such density-dependent weighting can extract additional cosmological information and tighten parameter constraints relative to the 2PCF alone [53–55].

A key obstacle in applying MCFs is the lack of accurate predictive models. Their nonlinear and environment-dependent nature precludes reliable analytic mappings from cosmological parameters to the statistic, while astrophysical and observational systematics—most notably galaxy bias—introduce additional uncertainties. These limitations motivate a simulation-based strategy, in which MCFs are measured across a suite of numerical simulations and interpolated over cosmological parameter space. This approach is enabled by emulators that combine large simulation suites with machine-learning techniques to provide fast and accurate predictions. Such methods were pioneered for the matter power spectrum by CosmicEmu [56–58], and have since been extended to smaller

*Electronic address: lixiaod25@mail.sysu.edu.cn

†Electronic address: yq_huang@sjtu.edu.cn

‡Electronic address: zhangle7@mail.sysu.edu.cn

¹ <https://desi.lbl.gov/>

² <https://www.lsst.org/>

³ <http://sci.esa.int/euclid/>

⁴ <https://roman.gsfc.nasa.gov/>

⁵ <http://nao.cas.cn/csst/>

scales, wider redshift ranges, and higher-dimensional parameter spaces [59, 60]. Emulators have also been developed for a range of large-scale structure observables, including the halo mass function [61], galaxy power spectra [62, 63], and the concentration–mass relation [64], as well as in recent large-scale emulation efforts [65–68].

In this work, we construct a simulation-based emulator for MCFs to use environmental clustering as a cosmological probe. Unlike the standard two-point correlation function, MCFs encode how clustering depends on local density and environmental transitions, making them sensitive to nonlinear structure formation and redshift-space anisotropies. We adopt a simulation-based inference approach [69], using forward simulations to learn the mapping between cosmological parameters and MCF statistics. This bypasses the need for an explicit analytic likelihood for marked statistics with non-trivial covariance and environmental weighting. We develop a Gaussian-process-regression (GPR) emulator for neighborhood-weighted MCFs in redshift space, trained on the KUN simulation suite and validated with independent JIUTIAN simulations.

The framework is designed to quantify the information gain from combining multiple mark powers α , test the complementarity between density-based and gradient-based marks, and assess the robustness of cosmological constraints to choices of scale range and halo selection. We focus on two reduced statistics, $\widehat{W}^\alpha(s)$ and $\widehat{W}_{\Delta_s}^\alpha(\mu)$, which retain the main scale-dependent and line-of-sight environmental information in a compact data vector.

The paper is organized as follows. Section II describes the simulation suites and tracer selection. Section III details the construction of the MCF estimators, the Gaussian process emulator, and the covariance modeling. Section IV presents the cosmological constraints and robustness analyses, comparing MCFs with the standard two-point correlation function. Finally, Section V summarizes our main findings and outlines future directions.

II. DATA

A. Kun simulation

We use the KUN simulation suite as the training set for the emulator [70]. The suite consists of 129 cosmologies spanning the $w_0w_a\text{CDM} + \sum m_\nu$ parameter space. Each realization is evolved with the GADGET-4 N -body solver⁶ [71] in a periodic box of side length $1 h^{-1}\text{Gpc}$ with 3072^3 particles, corresponding to a particle mass of $2.87 (\Omega_{cb}/0.3) \times 10^9 h^{-1}M_\odot$. The KUN suite is part of the JIUTIAN simulation program developed for CSST science [33, 72].

The cosmological parameter space spans baryon density Ω_b , matter density Ω_m , scalar spectral index n_s , Hubble

constant H_0 , primordial fluctuation amplitude A_s , dark energy equation-of-state parameters (w_0, w_a), and the summed neutrino mass $\sum m_\nu$, with ranges $\Omega_b \in [0.04, 0.06]$, $\Omega_m \in [0.24, 0.40]$, $n_s \in [0.92, 1.00]$, $H_0 \in [60, 80] \text{ km s}^{-1} \text{ Mpc}^{-1}$, $A_s \in [1.70, 2.50] \times 10^{-9}$, $w_0 \in [-1.30, -0.70]$, $w_a \in [-0.50, 0.50]$, and $\sum m_\nu \in [0.00, 0.30] \text{ eV}$.

The non-fiducial cosmologies are generated using a Sobol sequence [73], which provides a quasi-random, space-filling sampling of the high-dimensional parameter space for emulator training. Figure 1 illustrates this distribution: the 128 Sobol-sampled cosmologies (blue points) uniformly cover the parameter volume, while the fiducial *Planck* 2018 model [74] is shown as a red star. This homogeneous coverage minimizes clustering and voids in parameter space, thereby improving interpolation accuracy and reducing extrapolation in the likelihood analysis. Each cosmology is realized once; to suppress large-scale sample variance, the initial conditions adopt the fixed-amplitude method [75]. Halo and subhalo catalogs are identified using the ROCKSTAR algorithm [76], which are used to construct the tracer samples in this work.

B. Jiutian simulation

We use the primary JIUTIAN simulation both for covariance estimation and as an independent validation dataset [72]. It adopts a Planck 2018 ΛCDM cosmology with parameters $\Omega_m = 0.3111$, $\Omega_\Lambda = 0.6889$, $\Omega_b = 0.049$, $n_s = 0.9665$, $\sigma_8 = 0.8102$, and $H_0 = 67.66 \text{ km s}^{-1} \text{ Mpc}^{-1}$ [74]. The simulation evolves 6144^3 particles in a periodic box of side length $2 h^{-1}\text{Gpc}$. Halo and subhalo catalogs are identified using FoF and SUBFIND [77, 78].

To construct tracer samples, we impose a fixed number density $\bar{n} = 10^{-3} (h^{-1}\text{Mpc})^{-3}$ in all simulations by ranking halos and subhalos by mass and selecting the most massive objects. This corresponds to a characteristic mass threshold $M_{\text{cut}} \simeq 3.85 \times 10^{12} h^{-1}M_\odot$ for both KUN and JIUTIAN. By fixing \bar{n} , we control for variations in tracer abundance across cosmologies, ensuring that differences in the measured statistics arise mainly from clustering and environmental effects. The adopted number density is comparable to that expected in current and forthcoming spectroscopic galaxy surveys.

Redshift-space positions are constructed under the distant-observer approximation, taking the simulation z -axis as the line of sight:

$$\mathbf{s} = \mathbf{r} + \frac{\mathbf{v} \cdot \hat{\mathbf{z}}}{aH(a)} \hat{\mathbf{z}}, \quad (1)$$

where \mathbf{r} and \mathbf{s} denote the real- and redshift-space positions, \mathbf{v} is the peculiar velocity, a is the scale factor, and $H(a)$ is the Hubble parameter.

⁶ <https://wwwmpa.mpa-garching.mpg.de/gadget4/>

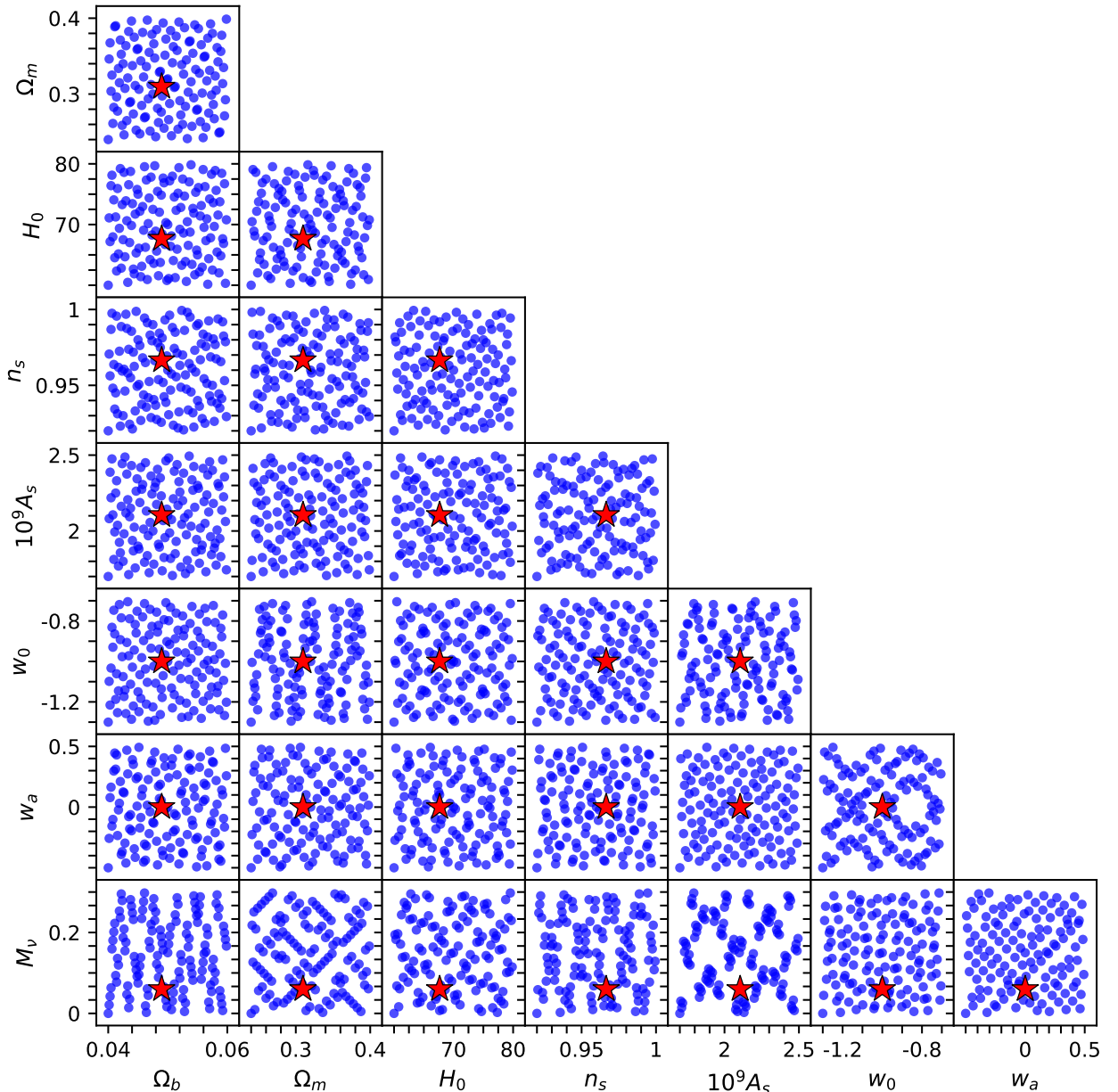


FIG. 1: Sampling of the 129 KUN cosmologies used to train the emulator. See also Figure 2 of Chen et al. [70]. Blue points show the 128 Sobol-sequence cosmologies, and the red star marks the fiducial *Planck* 2018 model. The broad parameter coverage ensures that the emulator operates primarily in the interpolation regime, thereby improving accuracy in the likelihood analysis.

III. METHODOLOGY

A. Construction of marked correlation functions (MCFs)

The purpose of MCFs is to supplement the ordinary two-point clustering signal with information about the local environment of each tracer. Instead of treating all halos equally, we assign each halo a mark that depends on its surrounding density field. Pair counts are then weighted by these marks, allowing the statistic to probe how clustering changes in dense regions,

underdense regions, or across environmental transitions.

We first define the local environment using an adaptive nearest-neighbor density,

$$\rho_{n_{\text{NB}}}(\mathbf{r}) = \sum_{i=1}^{n_{\text{NB}}} W_k(|\mathbf{r} - \mathbf{r}_i|, h_W), \quad (2)$$

where W_k is a third-order B-spline kernel with compact support inside $2h_W$ [79, 80]. The smoothing length h_W is chosen adaptively so that the kernel encloses the n_{NB} nearest neighbors around position \mathbf{r} . In this work we use $n_{\text{NB}} = 30$, which

gives $h_W = 8.3 \pm 3.7 h^{-1} \text{Mpc}$. The scale ($2h_W$) is thus close to the minimum pair separation used in the correlation measurement, $s_{\min} = 15 h^{-1} \text{Mpc}$. Therefore, the marks characterize quasi-nonlinear local environments, while the pair statistic is measured on larger clustering scales.

To capture not only dense regions but also spatial transitions between environments, we additionally compute the local density gradient,

$$\nabla \rho_{n_{\text{NB}}}(\mathbf{r}) = \sum_{i=1}^{n_{\text{NB}}} \nabla W_k(|\mathbf{r} - \mathbf{r}_i|, h_W). \quad (3)$$

The gradient is useful because cosmological information may not only reside in the density amplitude itself, but also in how rapidly the environment changes around halos.

1. Choice of marks

We use two environmental marks in the likelihood analysis. The first is the adaptive local density itself,

$$w = \rho_{n_{\text{NB}}}. \quad (4)$$

This mark directly upweights halos in dense environments. It is therefore sensitive to the clustering of halos in compact overdense structures.

The second mark is the normalized density gradient,

$$w = \frac{|\nabla \rho_{n_{\text{NB}}}|}{\rho_{n_{\text{NB}}}}. \quad (5)$$

This quantity measures the fractional change of the local density. Compared with the unnormalized gradient $|\nabla \rho_{n_{\text{NB}}}|$, it reduces the direct dependence on the density amplitude and is designed to highlight relative environmental transitions.

Figures 2 illustrate the motivation for using the normalized gradient rather than the raw gradient. The raw gradient is still strongly tied to high-density regions, whereas $|\nabla \rho_{n_{\text{NB}}}|/\rho_{n_{\text{NB}}}$ suppresses much of this density scaling. The two adopted marks therefore probe complementary environmental information: one traces dense regions directly, and the other emphasizes relative environmental variation.

2. Marked two-point statistic

We now incorporate the environmental marks into a two-point statistic. For a given mark w and mark power α , we define the marked correlation function as

$$W^\alpha(\mathbf{r}) = \langle \delta(\mathbf{x}) w^\alpha(\mathbf{x}) \delta(\mathbf{x} + \mathbf{r}) w^\alpha(\mathbf{x} + \mathbf{r}) \rangle. \quad (6)$$

Here δ is the tracer overdensity field, and the exponent α controls how strongly the mark affects the pair weighting.

For comparison, the ordinary two-point correlation function is

$$\xi(\mathbf{r}) = \langle \delta(\mathbf{x}) \delta(\mathbf{x} + \mathbf{r}) \rangle. \quad (7)$$

Thus, $\alpha = 0$ removes the mark weighting and recovers the standard unweighted two-point correlation function.

In redshift space, we estimate the marked statistic using the Landy-Szalay estimator,

$$W^\alpha(s, \mu) = \frac{WW(s, \mu) - 2WR(s, \mu) + RR(s, \mu)}{RR(s, \mu)}. \quad (8)$$

Here s is the pair separation and μ is the cosine of the angle between the pair separation vector and the line of sight. The quantities WW , WR , and RR denote normalized weighted data-data, data-random, and random-random pair counts, respectively. Random points are assigned unit mark, following the convention adopted in previous MCF analyses [53, 54].

The sign and magnitude of α determine which environments dominate the weighted pair counts. Positive values, such as $\alpha = 0.3$ and $\alpha = 0.5$, upweight high-mark regions. Negative values, such as $\alpha = -0.3$ and $\alpha = -0.5$, increase the relative contribution of low-mark regions. Therefore, varying α allows the statistic to scan different environmental regimes.

3. Scale and angular compression

The full two-dimensional statistic $W^\alpha(s, \mu)$ contains both scale dependence and line-of-sight angular dependence. To build a compact data vector, we compress it in two complementary ways.

First, to isolate the scale dependence, we integrate over the angular range,

$$W^\alpha(s) = \int_{\mu_{\min}}^{\mu_{\max}} W^\alpha(s, \mu) d\mu. \quad (9)$$

This statistic measures how the marked clustering amplitude varies with separation s after averaging over the selected angular range.

Second, to isolate the angular dependence, we integrate over the separation range,

$$W_{\Delta s}^\alpha(\mu) = \int_{s_{\min}}^{s_{\max}} W^\alpha(s, \mu) ds. \quad (10)$$

This statistic measures how the marked signal changes with orientation relative to the line of sight. It is therefore sensitive to anisotropic redshift-space effects.

Unless stated otherwise, all analyses use $s_{\min} = 15 h^{-1} \text{Mpc}$, $s_{\max} = 85 h^{-1} \text{Mpc}$, and $0 < \mu < 0.8$. With bin widths of $\Delta s = 10 h^{-1} \text{Mpc}$ and $\Delta \mu = 0.2$. These choices give 7 separation bins and 4 angular bins for each mark and each value of α .

4. Normalized marked correlation functions

For likelihood inference, we focus on the shape information rather than the overall integral of each marked statistic. We therefore define the normalized scale-dependent statistic as

$$\widehat{W}^\alpha(s) = \frac{W^\alpha(s)}{\int_{s_{\min}}^{s_{\max}} W^\alpha(s') ds'}. \quad (11)$$

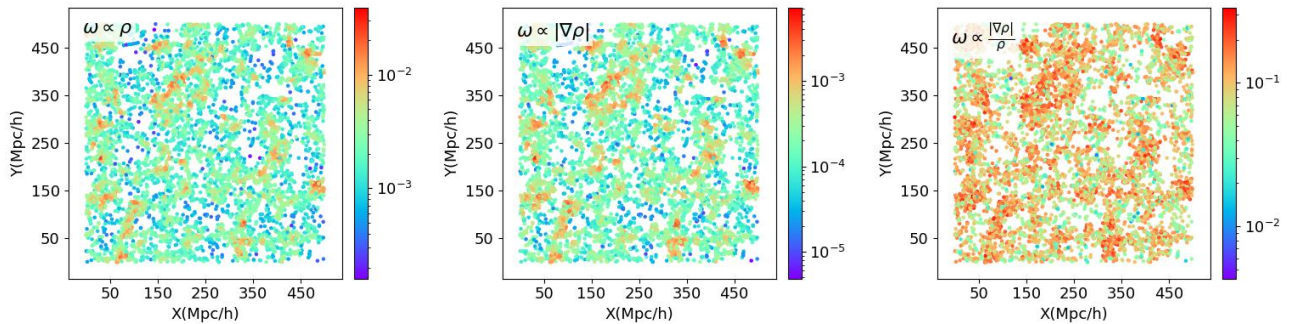


FIG. 2: Environmental quantities in a $500 \times 500 (h^{-1}\text{Mpc})^2$ slice of a KUN halo catalog. Left: the local-density mark ρ_{NB} , which emphasizes compact overdensities. Middle: the unnormalized gradient $|\nabla\rho_{\text{NB}}|$, which remains visually correlated with the density field because the largest gradients occur around dense structures. Right: the normalized gradient $|\nabla\rho_{\text{NB}}|/\rho_{\text{NB}}$, which reduces the direct density weighting and highlights relative environmental transitions.

Similarly, the normalized angular statistic is

$$\widehat{W}_{\Delta_S}^\alpha(\mu) = \frac{W_{\Delta_S}^\alpha(\mu)}{\int_{\mu_{\min}}^{\mu_{\max}} W_{\Delta_S}^\alpha(\mu') d\mu'}. \quad (12)$$

This normalization removes the total integrated amplitude of each statistic. The likelihood is therefore driven by changes in scale-dependent shape or angular-dependent shape. This choice is useful because it reduces sensitivity to an overall amplitude shift and emphasizes the relative redistribution of clustering signal across bins.

We build the final data vector by combining the normalized statistics from the two marks and five mark powers,

$$\alpha \in \{-0.5, -0.3, 0, 0.3, 0.5\}. \quad (13)$$

Here α controls the strength and direction of the environmental weighting. Positive values upweight high-mark regions, negative values give relatively more weight to low-mark regions, and $\alpha = 0$ reduces to the ordinary unweighted two-point statistic.

Figures 3 and 4 show the $\Delta\widehat{W}^\alpha(s) = \widehat{W}_{\text{kun}}^\alpha(s) - \widehat{W}_{\text{jiutian}}^\alpha(s)$ and $\Delta W_{\Delta_S}^\alpha(\mu) = W_{\Delta_S, \text{kun}}^\alpha(\mu) - W_{\Delta_S, \text{jiutian}}^\alpha(\mu)$ statistics. The marked statistics do not only change in overall amplitude as α varies. Their scale dependence and angular dependence also change. This is the key reason for using a multi-mark and multi- α data vector: different environmental weightings respond differently to cosmological parameters and can help break degeneracies that remain in the ordinary 2PCF.

B. Gaussian-process regression emulator

We use Gaussian-process regression (GPR) [81] to emulate the dependence of the marked correlation statistics on cosmological parameters. The goal is to obtain a fast and smooth prediction of the data vector at any cosmology within the training domain, without rerunning expensive simulations.

For a cosmological parameter vector $\hat{\theta}$, we denote one component of the MCF data vector by $w(\hat{\theta})$. In practice, the

same procedure is applied independently to each component of $\widehat{W}^\alpha(s)$ and $\widehat{W}_{\Delta_S}^\alpha(\mu)$. A Gaussian process places a prior distribution over functions,

$$f(\hat{\theta}) \sim \mathcal{GP}[m(\hat{\theta}), k(\hat{\theta}, \hat{\theta}')], \quad (14)$$

where $m(\hat{\theta})$ is the mean function and $k(\hat{\theta}, \hat{\theta}')$ is the covariance kernel. The simulated statistic is modeled as

$$w(\hat{\theta}) = f(\hat{\theta}) + \epsilon, \quad \epsilon \sim \mathcal{N}(0, \sigma_n^2), \quad (15)$$

where σ_n^2 represents the emulator noise term.

Given training cosmologies $\hat{\theta}$ and a test cosmology $\hat{\theta}_*$, the joint distribution of the training values f and the test value f_* is

$$\begin{bmatrix} f \\ f_* \end{bmatrix} \sim \mathcal{N} \left[\begin{bmatrix} m(\hat{\theta}) \\ m(\hat{\theta}_*) \end{bmatrix}, \begin{bmatrix} K(\hat{\theta}, \hat{\theta}) + \sigma_n^2 I & K(\hat{\theta}, \hat{\theta}_*) \\ K(\hat{\theta}_*, \hat{\theta}) & K(\hat{\theta}_*, \hat{\theta}_*) \end{bmatrix} \right], \quad (16)$$

where $K(\hat{\theta}, \hat{\theta})$ is the kernel matrix evaluated over all training cosmologies.

Conditioning on the training simulations gives a Gaussian predictive distribution,

$$f_* | \mathcal{D}, \hat{\theta}_* \sim \mathcal{N}(\bar{f}_*, \text{Cov}(f_*)), \quad (17)$$

where $\mathcal{D} = \{\hat{\theta}, w\}$ denotes the training cosmologies and their simulated statistics. The predictive mean is

$$\bar{f}_* = m(\hat{\theta}_*) + K(\hat{\theta}_*, \hat{\theta}) [K(\hat{\theta}, \hat{\theta}) + \sigma_n^2 I]^{-1} [w - m(\hat{\theta})], \quad (18)$$

and the predictive covariance is

$$\text{Cov}(f_*) = K(\hat{\theta}_*, \hat{\theta}_*) - K(\hat{\theta}_*, \hat{\theta}) [K(\hat{\theta}, \hat{\theta}) + \sigma_n^2 I]^{-1} K(\hat{\theta}, \hat{\theta}_*). \quad (19)$$

The predictive mean \bar{f}_* is used as the emulator prediction, while the predictive covariance quantifies the interpolation uncertainty.

We compare three kernel choices. The first is the radial basis function (RBF) kernel,

$$k_{\text{RBF}}(\hat{\theta}_i, \hat{\theta}_j) = \sigma_f^2 \exp\left(-\frac{r_{ij}^2}{2l^2}\right), \quad (20)$$

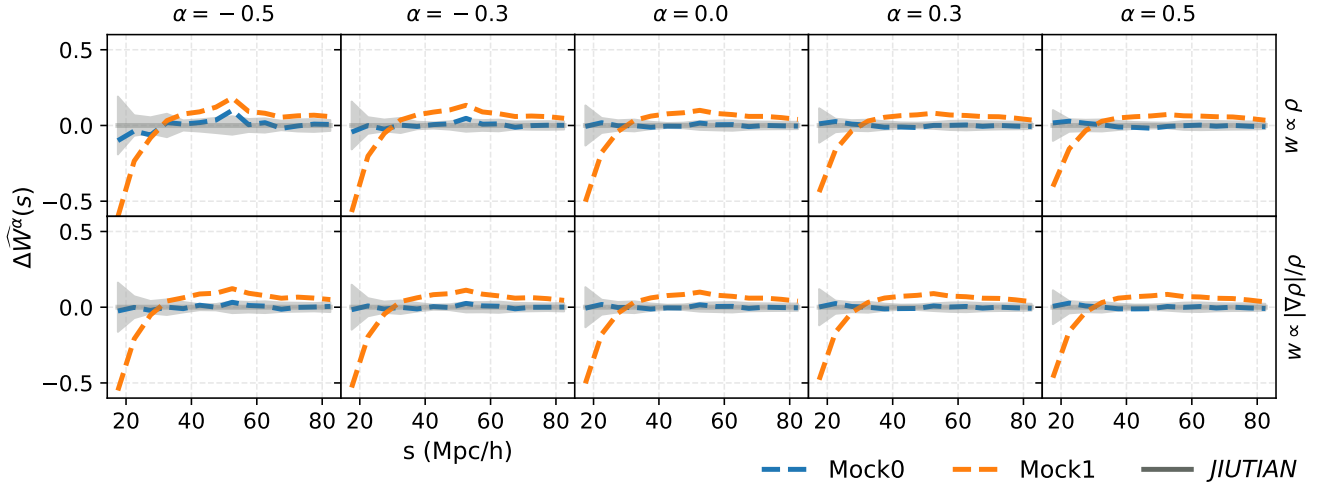


FIG. 3: Scale-dependent marked statistic $\Delta\widehat{W}^\alpha(s)$ at $z = 0.5$, defined as the difference between the KUN simulations and a $(600 h^{-1}\text{Mpc})^3$ subsample of JIUTIAN. The gray shaded region shows the 1σ uncertainty. The blue and yellow dashed lines correspond to the fiducial (Mock0) and nonfiducial (Mock1) cosmologies from KUN, respectively. The upper and lower rows use $w = \rho_{\text{NB}}$ and $w = |\nabla\rho_{\text{NB}}|/\rho_{\text{NB}}$, while columns show $\alpha = -0.5, -0.3, 0, 0.3, 0.5$. The agreement between JIUTIAN and the fiducial KUN confirms consistency at fixed cosmology, whereas the nonfiducial case shows clear deviations. The distinct scale dependence across different α values motivates the joint multi- α analysis.

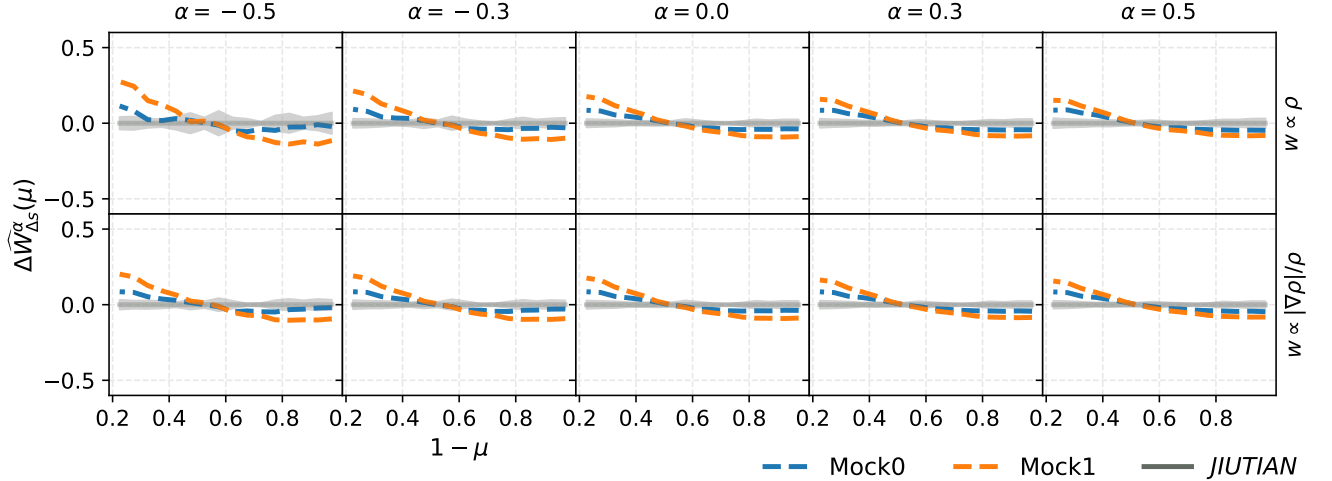


FIG. 4: Angular marked statistic $\Delta W_{\Delta s}^\alpha(\mu)$, shown as a function of $1 - \mu$, for the same mark choices and simulations as in Figure 3. Compared with $W^\alpha(s)$, the dependence on α is less pronounced in amplitude, but the systematic variations across angular bins remain sensitive to cosmological parameters.

where

$$r_{ij} = \|\hat{\theta}_i - \hat{\theta}_j\|. \quad (21)$$

The RBF kernel assumes a very smooth dependence on cosmological parameters.

The second is the Matérn kernel with $\nu = 5/2$ (M52),

$$k_{\text{M52}}(\hat{\theta}_i, \hat{\theta}_j) = \sigma_f^2 \left(1 + \frac{\sqrt{5}r_{ij}}{l} + \frac{5r_{ij}^2}{3l^2} \right) \exp\left(-\frac{\sqrt{5}r_{ij}}{l}\right). \quad (22)$$

Compared with the RBF kernel, the M52 kernel allows less restrictive smoothness while still producing sufficiently regular

functions. This flexibility is useful when the statistic varies nontrivially across cosmological parameter space. Previous work has also found that the M52 kernel can outperform the RBF kernel for cosmological emulation tasks [82].

The third kernel is a product kernel (M52-RBF),

$$k_{\text{M52-RBF}}(\hat{\theta}_i, \hat{\theta}_j) = k_{\text{M52}}(\hat{\theta}_i, \hat{\theta}_j)k_{\text{RBF}}(\hat{\theta}_i, \hat{\theta}_j). \quad (23)$$

This composite kernel combines the flexibility of the M52 kernel with the smoothness of the RBF kernel, and is included to test whether a more structured covariance model improves emulator accuracy.

In the following analysis, we train the GPR emulator on the

KUN simulation suite and validate its predictions using independent JIUTIAN simulations. The comparison among kernels allows us to identify a stable emulator model for the normalized MCF data vectors used in the likelihood analysis.

In practice, we include an overall amplitude parameter,

$$K(\hat{\theta}_i, \hat{\theta}_j) = A_c k(\hat{\theta}_i, \hat{\theta}_j), \quad (24)$$

where A_c rescales the covariance amplitude, and k denotes one of the RBF, M52, or M52-RBF kernels.

The training process in GPR is to find the optimal hyperparameters for the given training data and kernel function. This is achieved by the optimization of the log marginal likelihood of the input data via maximizing

$$\begin{aligned} \ln \mathcal{L}_{\text{GPR}} = & -\frac{1}{2} f^\top [K(\hat{\theta}, \hat{\theta}) + \sigma_n^2 I]^{-1} f \\ & -\frac{1}{2} \log |K(\hat{\theta}, \hat{\theta}) + \sigma_n^2 I| - \frac{n}{2} \log 2\pi. \end{aligned} \quad (25)$$

Here n is the dimension of cosmological parameter space. We implement the GPR emulator with the Python package SCIKIT-LEARN [83]. The emulator is trained separately for each component of the normalized MCF data vector and then used to predict the statistics at new cosmological parameters.

We compare the RBF, M52, and M52-RBF kernels using the independent JIUTIAN validation simulations. All three kernels provide accurate predictions, and their validation errors differ by less than 5%. This indicates that the emulator performance is not sensitive to the kernel choice for the present data vector. We therefore adopt the RBF kernel as the fiducial emulator in the following analysis, because it is simple, stable, and sufficient for the required interpolation accuracy.

To assess the generalization accuracy of the emulator, we perform leave-one-out (LOO) cross-validation. This test is useful for our relatively small simulation set because each simulation is used once as the validation sample, while all remaining simulations are used for training. Repeating this procedure over all simulations gives an estimate of the emulator error across the training cosmologies.

For each bin of the data vector, we define the LOO error as the 68th-percentile fractional error over all validation samples. As shown in Figure 5, the emulator achieves fractional errors below 8% for the scale-dependent statistic $\widehat{W}^\alpha(s)$ and below 1.5% for the angular statistic $\widehat{W}_{\Delta s}^\alpha(\mu)$ across the tested values of α . These small errors indicate that the emulator accurately interpolates the MCF statistics across the cosmological parameter space covered by the training simulations.

We also observe that the errors for negative mark powers, especially $\alpha = -0.5$ and $\alpha = -0.3$, are generally larger than those for $\alpha = 0$ and $\alpha > 0$. This behavior is expected because negative α values give relatively more weight to low-mark environments. These regions contain fewer tracers and are therefore more affected by shot noise, leading to slightly larger emulator uncertainties.

C. Covariance estimation and likelihood

The Gaussian-process emulator provides predictions for the marked-correlation data vector at arbitrary cosmologies within the training range. We next describe the covariance matrix and likelihood used for parameter inference. We denote the full data vector by $\mathbf{y} = \widehat{W}^\alpha(s)$ or $\mathbf{y} = \widehat{W}_{\Delta s}^\alpha(\mu)$, including all selected mark definitions, mark powers α , and separation or angular bins. For a cosmological parameter vector $\boldsymbol{\theta}$, the emulator prediction is denoted by $\mathbf{y}_{\text{emu}}(\boldsymbol{\theta})$. Assuming a Gaussian likelihood, we adopt

$$\ln \mathcal{L}(\boldsymbol{\theta}) = -\frac{1}{2} \Delta \mathbf{y}^\top \mathbf{C}^{-1} \Delta \mathbf{y} + \text{const.}, \quad (26)$$

where

$$\Delta \mathbf{y} = \mathbf{y}_{\text{obs}} - \mathbf{y}_{\text{emu}}(\boldsymbol{\theta}). \quad (27)$$

Here \mathbf{y}_{obs} is the measured data vector, and $\mathbf{y}_{\text{emu}}(\boldsymbol{\theta})$ is the phase-corrected emulator prediction defined below. Since the covariance matrix is fixed in our analysis, the normalization term of the Gaussian likelihood does not affect parameter inference and is absorbed into the constant.

The total covariance is modeled as

$$\mathbf{C} = \mathbf{C}_{\text{data}} + \mathbf{C}_{\text{emu}}. \quad (28)$$

The first term describes the statistical uncertainty of the measured data vector, while the second term accounts for interpolation errors from the emulator. The effect of the fixed initial phase in the training simulations is treated as a correction to the emulator mean prediction, rather than as an additional covariance term.

1. Data covariance

We estimate the data covariance from subvolumes of the JIUTIAN simulation. The full simulation is divided into $N_{\text{sub}} = 5^3 = 125$ subsamples, each with volume $V_{\text{sub}} = (400 h^{-1} \text{Mpc})^3$. Let \mathbf{y}_k be the data vector measured from the k -th subvolume, and let

$$\bar{\mathbf{y}} = \frac{1}{N_{\text{sub}}} \sum_{k=1}^{N_{\text{sub}}} \mathbf{y}_k \quad (29)$$

be the mean over all subvolumes. The covariance for an observed volume V_{obs} is then estimated as

$$\mathbf{C}_{\text{data}} = \frac{V_{\text{sub}}}{V_{\text{obs}}} \frac{1}{N_{\text{sub}} - 1} \sum_{k=1}^{N_{\text{sub}}} (\mathbf{y}_k - \bar{\mathbf{y}}) (\mathbf{y}_k - \bar{\mathbf{y}})^\top. \quad (30)$$

The factor $V_{\text{sub}}/V_{\text{obs}}$ rescales the covariance from the subvolume size to the target observational volume.

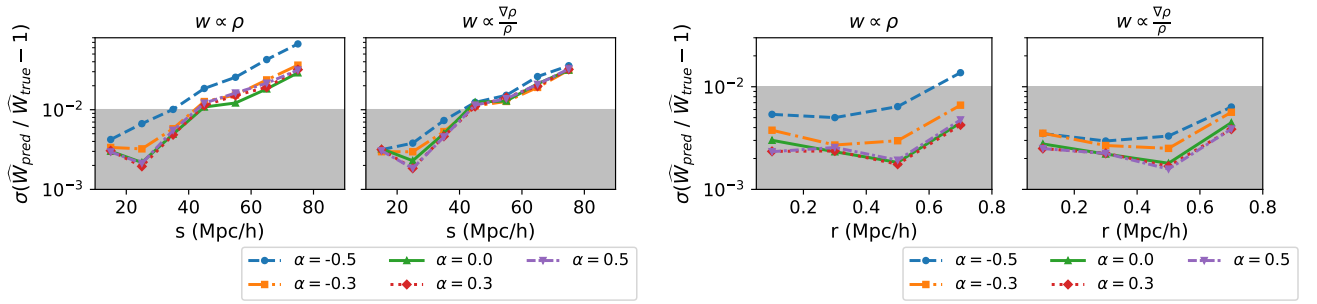


FIG. 5: Leave-one-out validation errors of the GPR emulator. The left panel shows the 68th-percentile fractional error for the scale-dependent statistic $\widehat{W}^\alpha(s)$, while the right panel shows the corresponding error for the angular statistic $\widehat{W}_{\Delta s}^\alpha(\mu)$. The shaded regions indicate errors below 1%. Different curves correspond to different mark powers α .

2. Emulator covariance

The emulator covariance quantifies the uncertainty introduced by interpolation across cosmological parameter space. We estimate this term using the leave-one-out validation described in the previous section. For the j -th training cosmology, the emulator is trained on all other cosmologies and then evaluated at the omitted point. The residual vector is

$$\mathbf{e}_j = \mathbf{y}_{\text{emu}}^{(-j)}(\boldsymbol{\theta}_j) - \mathbf{y}_{\text{true}}(\boldsymbol{\theta}_j), \quad (31)$$

where $\mathbf{y}_{\text{emu}}^{(-j)}$ is the leave-one-out emulator prediction and \mathbf{y}_{true} is the statistic measured directly from the simulation.

The emulator covariance is estimated from these residuals:

$$\mathbf{C}_{\text{emu}} = \frac{1}{N_{\text{train}} - 1} \sum_{j=1}^{N_{\text{train}}} (\mathbf{e}_j - \bar{\mathbf{e}}) (\mathbf{e}_j - \bar{\mathbf{e}})^T, \quad (32)$$

where

$$\bar{\mathbf{e}} = \frac{1}{N_{\text{train}}} \sum_{j=1}^{N_{\text{train}}} \mathbf{e}_j. \quad (33)$$

In practice, we find that \mathbf{C}_{emu} is much smaller than \mathbf{C}_{data} , indicating that emulator interpolation errors are subdominant compared with the statistical uncertainty of the data vector.

3. Correction for fixed initial phases

The KUN training simulations are generated with fixed initial phases. While this suppresses sample variance and improves emulator training, it can introduce a systematic offset between the emulator prediction and the ensemble-averaged statistic from independent realizations. Following the ratio-based correction [84], we account for this effect by rescaling the emulator mean prediction.

We define the bin-wise correction factor as

$$R_i = \frac{\bar{y}_{\text{Jiutian},i}}{y_{\text{Kun},\text{fid},i}}, \quad (34)$$

where $\bar{y}_{\text{Jiutian},i}$ is the ensemble mean measured from the independent JIUTIAN realizations, and $y_{\text{Kun},\text{fid},i}$ is the fiducial measurement from KUN. We then rescale the emulator prediction as

$$y_{\text{emu},i}(\boldsymbol{\theta}) \rightarrow R_i y_{\text{emu},i}(\boldsymbol{\theta}). \quad (35)$$

This procedure assumes that the fixed-phase bias is only weakly dependent on cosmology, so that the ratio R_i estimated at the fiducial cosmology can be applied across parameter space. We therefore use y_{model} as the fiducial prediction in the likelihood analysis. Since the residual phase uncertainty is subdominant compared with the statistical covariance, no additional phase-covariance term is included.

The likelihood uses the full covariance matrix of the data vector, which fully captures correlations between all elements. Because the data vector combines multiple bins, marks, and mark powers, the covariance between elements is non-negligible and must be fully retained. Correlations arise both from neighboring separation (or angular) bins and from the two marks, which trace related properties of the same underlying density field.

Figure 6 shows substantial off-diagonal structure, indicating that many bins are strongly correlated. Increasing the number of bins would therefore not proportionally increase the independent information content, but would instead amplify noise in the estimated covariance and degrade matrix inversion. For this reason, we adopt a coarse binning scheme for both $\widehat{W}^\alpha(s)$ and $\widehat{W}_{\Delta s}^\alpha(\mu)$. This balances information retention against covariance stability, ensuring robust parameter inference with the available simulation volume.

4. Inverse covariance correction

Because the covariance matrix is estimated from a finite number of subvolumes, its inverse is biased. We correct this bias using the Hartlap factor [85]. The debiased inverse covariance is

$$\widehat{\mathbf{C}}^{-1} = \frac{N_{\text{sub}} - N_d - 2}{N_{\text{sub}} - 1} \mathbf{C}^{-1}, \quad (36)$$

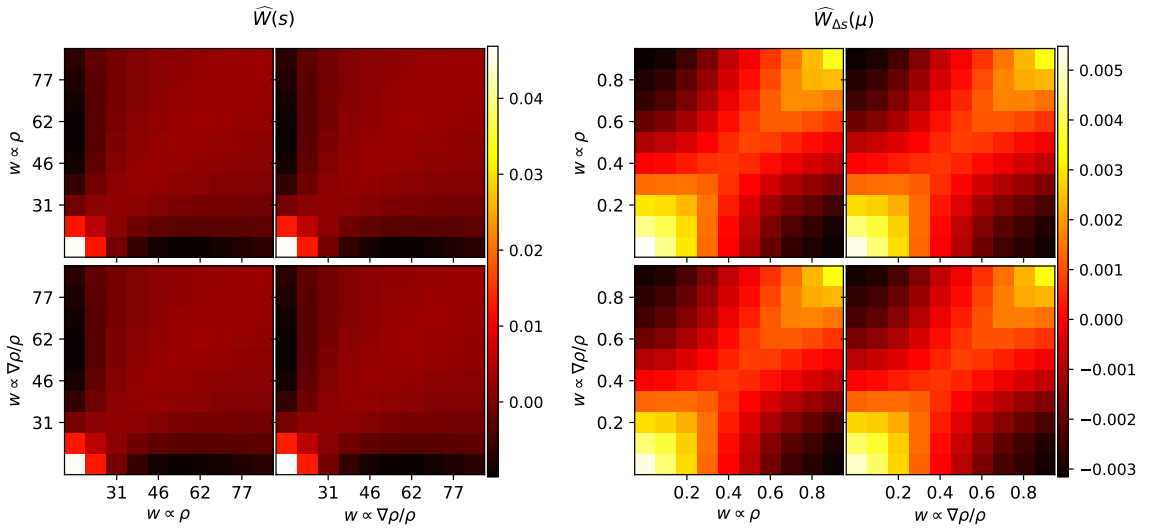


FIG. 6: Covariance matrices for $\widehat{W}^\alpha(s)$ (left) and $\widehat{W}_{\Delta s}^\alpha(\mu)$ (right) for the representative mark power $\alpha = 0.5$. Strong within-mark correlations are visible, together with non-negligible cross-correlations between $w \propto \rho_{\text{NB}}$ and $w \propto |\nabla \rho_{\text{NB}}|/\rho_{\text{NB}}$. The overall covariance amplitude is larger for $\widehat{W}^\alpha(s)$, with maxima of approximately 8×10^{-3} and 1.25×10^{-3} , respectively.

where N_d is the dimension of the data vector. This correction is well defined only when $N_{\text{sub}} > N_d + 2$, which motivates the compact binning scheme adopted for the MCF data vector.

IV. RESULTS

A. Comparison of 2PCF and MCFs

We quantify the constraining power of MCFs relative to the standard 2PCF, considering both individual marks and their combinations. Since correlation statistics are primarily sensitive to the matter density Ω_m and the fluctuation amplitude σ_8 , and these two parameters exhibit a strong degeneracy in such measurements, we perform the cosmological inference in the Ω_m - σ_8 plane.

As a validation dataset, we use a $(600 h^{-1} \text{Mpc})^3$ sub-volume of the JIUTIAN simulation, which provides an independent realization at the fiducial cosmology. Likelihood evaluations are performed using the emulator described in Section III, and posterior sampling is carried out with the EMCEE package [86].

Figure 7 presents the resulting 1σ constraints on Ω_m and σ_8 , derived from the 2PCF and from MCFs with different choices of the mark exponent α (visualized using GETDIST [87]). Results are shown for both the scale-dependent statistic $\widehat{W}^\alpha(s)$ (left panel) and the angular statistic $\widehat{W}_{\Delta s}^\alpha(\mu)$ (right panel).

Several trends are apparent. First, a single marked statistic (fixed α) provides constraints that are comparable to, but not significantly stronger than, the standard 2PCF ($\alpha = 0$). Second, combining multiple α values leads to a clear improvement. In particular, both the three-weight combination $\alpha = \{-0.3, 0, 0.3\}$ and the full set $\alpha = \{-0.5, -0.3, 0, 0.3, 0.5\}$ tighten the contours relative to the 2PCF alone, with the full combination yielding the strongest constraints.

This behavior reflects the complementary information encoded by different marks: positive α emphasizes overdense environments, while negative α enhances the contribution from underdense regions. Combining them probes clustering across a wide range of environments, helping to break degeneracies in the unweighted statistic. Overall, these results demonstrate that the gain from MCFs does not arise from any single weighting scheme, but from their joint use as a multi-component summary statistic.

The improvement is first evident in the one-dimensional posteriors shown in Figure 8. For $\widehat{W}^\alpha(s)$, combining three weights ($\alpha = \{-0.3, 0, 0.3\}$) reduces the 1σ uncertainties by $\sim 41\%$ for Ω_m and $\sim 47\%$ for σ_8 relative to the standard 2PCF. Including all five weights further changes the constraints, giving reductions of $\sim 38\%$ and $\sim 33\%$, respectively. Although the full five-weight combination yields slightly weaker statistical constraints than the three-weight case, it produces smaller shifts in the best-fit parameters relative to the true cosmology: the bias in Ω_m decreases from 0.20 to 0.08, and that in σ_8 from 0.007 to 0.002. For the angular statistic $\widehat{W}_{\Delta s}^\alpha(\mu)$, the corresponding reductions are 13% and 25% (three weights), and 45% and 36% (five weights). These results indicate that combining multiple α values substantially improves constraining power compared to any single statistic. Overall, we adopt the full five-weight combination as the baseline choice, as it provides a good balance between statistical precision and robustness.

To quantify joint constraints including parameter degeneracies, we adopt the Figure of Merit (FoM) defined as the inverse square root of the covariance determinant [88],

$$\text{FoM} \equiv \frac{1}{\sqrt{\det \mathbf{C}}}. \quad (37)$$

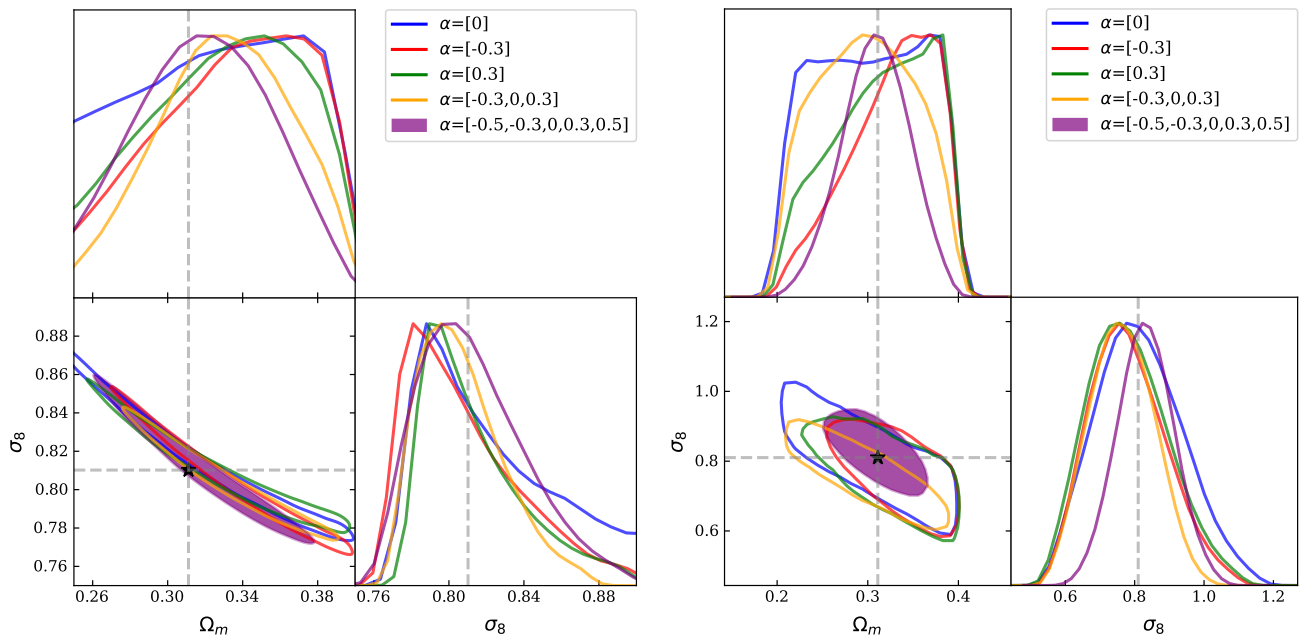


FIG. 7: Comparison of 1σ posterior contours for Ω_m and σ_8 , derived from the standard 2PCF and MCFs with different α values. Dashed lines indicate the fiducial values $\Omega_m = 0.311$ and $\sigma_8 = 0.81$.

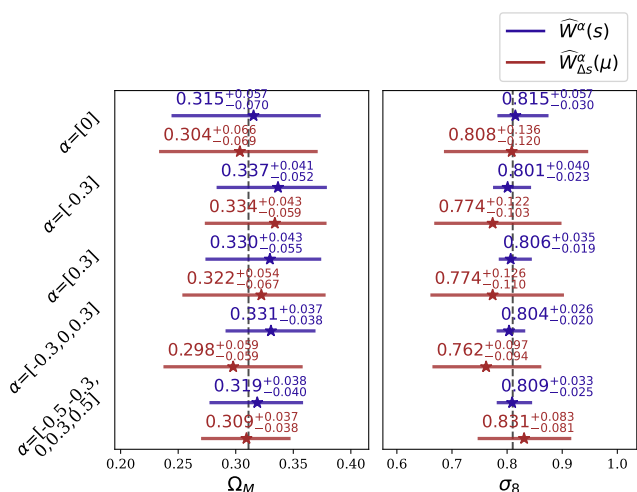


FIG. 8: 1D posteriors for Ω_m and σ_8 from the 2PCF and MCFs (varying α). Dashed lines mark the fiducial values.

For the two parameters (Ω_m - σ_8), this becomes

$$\text{FoM} = \frac{1}{\sigma(\Omega_m) \sigma(\sigma_8) \sqrt{1 - \rho^2}}, \quad (38)$$

where ρ denotes the correlation coefficient between Ω_m and σ_8 . This form directly reflects the inverse area of the error ellipse and generalizes to higher dimensions via $\det \mathbf{C}$.

Table IV A summarizes the FoM for different α configurations, normalized to the five-weight $\widehat{W}^\alpha(s)$ case. Compared to the 2PCF-only case ($\alpha = 0$), the three-weight combination ($\alpha = [-0.3, 0, 0.3]$) increases the FoM by factors of ~ 2.51

for $\widehat{W}^\alpha(s)$ and ~ 1.70 for $\widehat{W}_{\Delta s}^\alpha(\mu)$. Including all five weights ($\alpha = [-0.5, -0.3, 0, 0.3, 0.5]$) yields FoM gains of ~ 1.90 and ~ 2.39 , respectively. We find that for $\widehat{W}^\alpha(s)$, the configuration using a single negative weight ($\alpha = -0.3$) yields a larger FoM than the full five-weight combination. However, as shown in Figure 7, this case exhibits stronger parameter degeneracies, resulting in biased posteriors where the 1σ contours do not fully recover the true cosmology.

Taken together, these results show that the primary gain from MCFs arises from combining multiple environmental weightings, which effectively reduces both parameter uncertainties and degeneracies, leading to a substantially smaller allowed parameter volume.

	$\widehat{W}_{\Delta s}^\alpha(\mu)$	$\widehat{W}^\alpha(s)$
$\alpha = [0]$	0.044	0.525
$\alpha = [-0.3]$	0.059	1.060
$\alpha = [0.3]$	0.049	0.788
$\alpha = [-0.3, 0, 0.3]$	0.075	1.320
$\alpha = [-0.5, -0.3, 0, 0.3, 0.5]$	0.105	1.000

TABLE I: FoM for various α values, normalized to the $\widehat{W}^\alpha(s)$ FoM for the fiducial combination $\alpha = \{-0.5, -0.3, 0, 0.3, 0.5\}$.

The composite parameter

$$S_8 \equiv \sigma_8 \left(\frac{\Omega_m}{0.3} \right)^{1/2}, \quad (39)$$

shows a similar trend. For the standard 2PCF ($\alpha = 0$), we obtain $S_8 = 0.804 \pm 0.093$, consistent with the fiducial value $S_8^{\text{fid}} \simeq 0.825$ within 1σ . Single marked statistics with $\alpha = -0.3$

and $\alpha = 0.3$ yield comparable central values and uncertainties. However, the three-weight combination $\alpha = \{-0.3, 0, 0.3\}$ shifts the posterior to $S_8 = 0.75 \pm 0.061$, corresponding to a $\sim 2\sigma$ deviation from the fiducial value, despite the reduced statistical uncertainty. In contrast, the full five-weight combination $\alpha = \{-0.5, -0.3, 0, 0.3, 0.5\}$ recovers $S_8 = 0.836 \pm 0.062$, in excellent agreement with the fiducial cosmology, while still achieving a $\sim 33\%$ reduction in the 1σ uncertainty relative to the 2PCF.

These results indicate that although combining a small number of marked statistics improves precision, it can introduce systematic shifts in degenerate parameter combinations such as S_8 . A wider range of α values is therefore required to achieve both high precision and unbiased parameter recovery.

B. Impact of weighting scheme and scale cuts on MCF constraints

In this section, we study how the cosmological constraints from MCFs depend on key analysis choices, in particular the weighting scheme and the range of separation scales s . Unless otherwise specified, all results use the five-weight combination $\alpha = [-0.5, -0.3, 0, 0.3, 0.5]$.

TABLE II: FoM for different marker schemes. All FoM values are normalized to that of $\widehat{W}^\alpha(s)$ with the joint weighting configuration $w \propto |\nabla\rho|/\rho$ and $w \propto \rho$, which is set to unity for reference.

	$w \propto \nabla\rho /\rho$	$w \propto \rho$	Joint
$\widehat{W}_{\Delta s}^\alpha(\mu)$	0.078	0.073	0.105
$\widehat{W}^\alpha(s)$	1.086	1.168	1.000

TABLE III: FoM for different choices of the separation range s . All values are normalized to the FoM of the isotropic statistic $\widehat{W}^\alpha(s)$ with $s \in [15, 65] h^{-1}\text{Mpc}$, which is set to unity.

$s \in$	[15, 85]	[15, 75]	[25, 85]	[15, 95]
$\widehat{W}_{\Delta s}^\alpha(\mu)$	0.105	0.110	0.094	0.098
$\widehat{W}^\alpha(s)$	1.00	0.755	1.39	1.30

Figure 9 compares the cosmological constraints obtained using two weighting schemes, $w \propto \rho$ and $w \propto |\nabla\rho|/\rho$, as well as their joint combination. For the isotropic statistic $\widehat{W}^\alpha(s)$, the joint analysis yields constraints on Ω_m and σ_8 that are comparable to those obtained from the best single-weight case, as quantified by the FoM values in Table II. The joint FoM is approximately 14% lower than that of $w \propto \rho$ alone, indicating that the two weighting schemes are strongly correlated in the isotropic MCF and therefore provide largely redundant information. Nevertheless, the joint combination slightly improves the constraint on σ_8 , while leading to a marginally larger shift in Ω_m toward the fiducial value, reflecting a partial reduction in parameter degeneracies.

A much stronger improvement is found when using the anisotropic statistic $\widehat{W}_{\Delta s}^\alpha(\mu)$. In this case, the joint analysis tightens the marginalized constraints by approximately 35%

for Ω_m and 11% for σ_8 , as shown in Figure 11. Consistently, the FoM increases by a factor of ~ 1.4 compared with either individual weighting scheme. These results indicate that the anisotropic MCF captures more complementary information from different environmental weights. In other words, once the angular dependence with respect to the line of sight is retained, the two weighting schemes become less redundant and their combination substantially improves the overall constraining power.

We next examine how the constraints depend on the separation range s , as shown in Figures 10 and 12. We consider four configurations: $s \in [15, 75]$, $[15, 85]$, $[15, 95]$, and $[25, 85] h^{-1}\text{Mpc}$.

For the isotropic statistic $\widehat{W}^\alpha(s)$, the constraining power depends sensitively on the adopted separation range. Reducing s_{max} from 85 to 75 $h^{-1}\text{Mpc}$ leads to a significant decrease in the FoM of approximately 24% (see Table III). In contrast, either increasing s_{min} from 15 to 25 $h^{-1}\text{Mpc}$ or extending s_{max} to 95 $h^{-1}\text{Mpc}$ improves the FoM by $\sim 39\%$ and $\sim 30\%$, respectively. However, these gains in statistical precision are accompanied by increased parameter bias relative to the fiducial cosmology ($\Omega_m = 0.31$, $\sigma_8 = 0.81$). As shown in Figure 12, for the range $s \in [25, 85] h^{-1}\text{Mpc}$, the relative biases in both Ω_m and σ_8 are approximately twice as large as those obtained from the baseline $s \in [15, 85] h^{-1}\text{Mpc}$. For the case $s \in [15, 95] h^{-1}\text{Mpc}$, the bias in Ω_m increases by a factor of about three relative to the baseline, while the increase in the σ_8 bias is more moderate. These results highlight a trade-off between statistical constraining power and robustness to systematic shifts when incorporating larger separation scales.

For the anisotropic statistic $\widehat{W}_{\Delta s}^\alpha(\mu)$, the constraining power is primarily driven by the inclusion of small scales. The FoM is strongly degraded when s_{min} is increased to 25 $h^{-1}\text{Mpc}$, whereas varying s_{max} within the tested range has only a minor effect. This suggests that the anisotropic MCF gains most of its cosmological sensitivity from quasi-linear to mildly nonlinear scales, while the additional large-scale information contributes only subdominantly.

Overall, these results show that the constraining power of MCFs is mainly controlled by two factors: the inclusion of redshift-space anisotropy and the retention of small-scale information. Combining multiple marks provides an additional gain, but this gain is subdominant compared with the improvement obtained from the anisotropic statistic and from the small-scale separation bins.

C. Impact of Halo Bias on Cosmological Constraints

To test the robustness of our method against uncertainties in how tracers relate to the underlying matter distribution, we evaluate its performance on mock halo catalogs constructed with different halo mass selections, while keeping the emulator training data unchanged. Specifically, we impose three truncation mass thresholds, $M_{\text{cut}} = 3.85 \times 10^{12}$, 3.15×10^{12} , and $1.65 \times 10^{12} M_\odot$, on the original halo catalog. For each value of M_{cut} , we further randomly remove 0%, 20%, 60% of halos/subhalos to maintain a constant number density. This

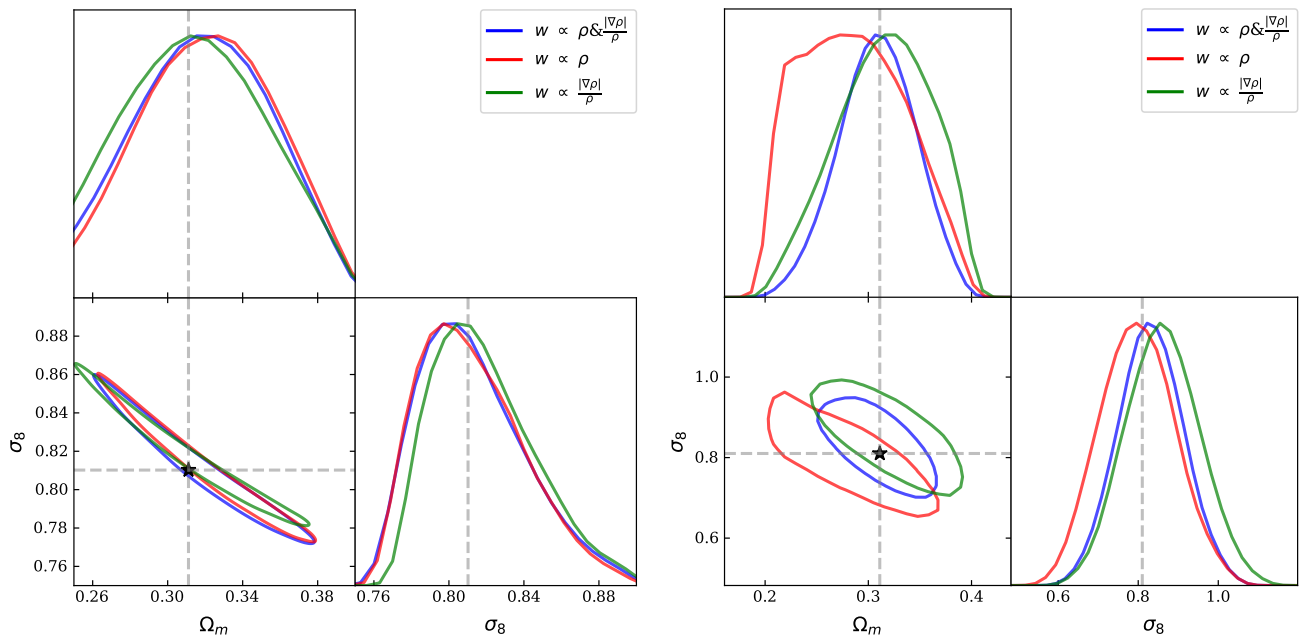


FIG. 9: The MCMC results for $\widehat{W}^\alpha(s)$ (left) and $\widehat{W}_{\Delta s}^\alpha(\mu)$ (right). For all cases, we adopt the same set of mark parameters $\alpha = [-0.5, -0.3, 0, 0.3, 0.5]$, and perform a joint combination of the corresponding contributions across these α values. We compare different weighting schemes, including $w \propto \rho$ and $w \propto \nabla\rho/\rho$, all evaluated under the fiducial binning scheme.

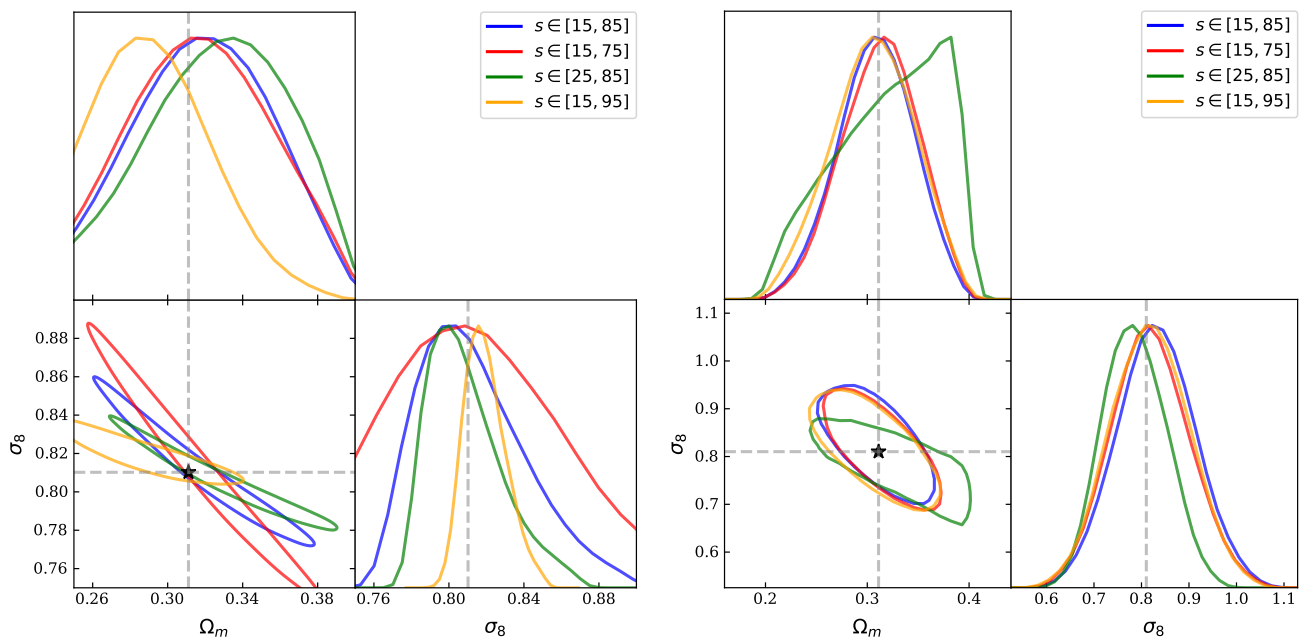


FIG. 10: Similar to Figure 9, but showing results for different choices of the separation range s : $[15, 75]$, $[15, 85]$, $[25, 85]$, and $[15, 95] h^{-1}\text{Mpc}$. The binning scheme is kept fixed with the fiducial choices $\Delta s = 10 h^{-1}\text{Mpc}$ and $\mu \in [0, 0.8]$ with $\Delta\mu = 0.2$, respectively.

procedure isolates the impact of changes in the internal halo population (i.e., mass-dependent tracer properties) from variations in the overall clustering amplitude.

As shown in Figure 13, the cosmological constraints derived from $\widehat{W}^\alpha(s)$ and $\widehat{W}_{\Delta s}^\alpha(\mu)$ remain highly consistent across all

halo samples. The posterior shifts in both Ω_m and σ_8 are within 1σ of the fiducial case, indicating strong insensitivity to the adopted halo mass range. Quantitatively, relative to the fiducial case ($M_{\text{cut}} = 3.85 \times 10^{12} M_\odot$), the FoM of $\widehat{W}^\alpha(s)$ and $\widehat{W}_{\Delta s}^\alpha(\mu)$ changes within 10% for $M_{\text{cut}} = 3.15 \times 10^{12}$ and $1.65 \times 10^{12} M_\odot$.

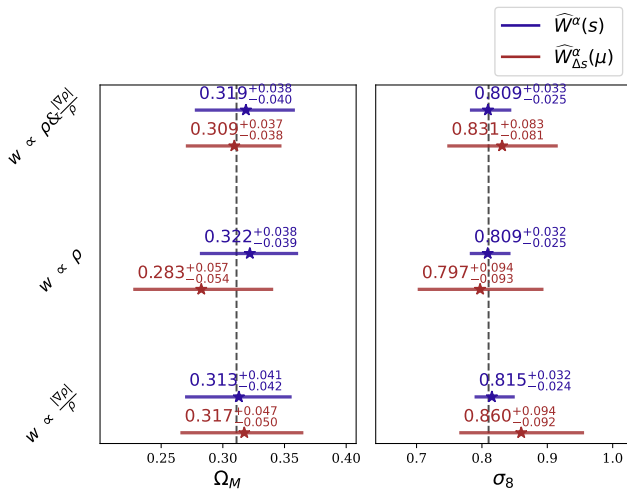


FIG. 11: Same configurations as in Figure 9, but presenting the marginalized one-dimensional MCMC constraints.

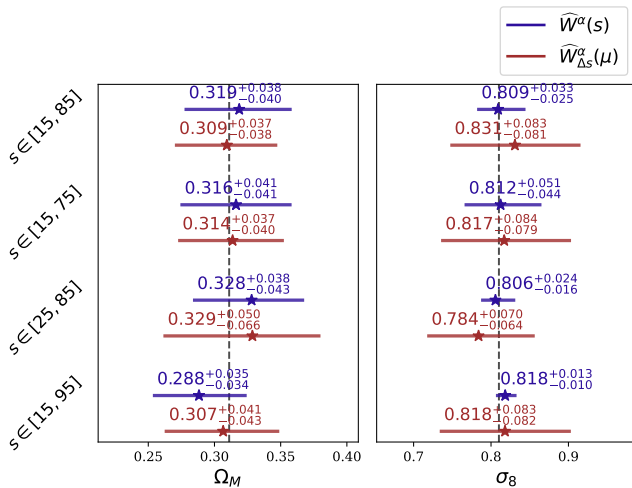


FIG. 12: Same configurations as in Figure 10, but presenting the one-dimensional marginalized MCMC constraints.

This demonstrates that $\widehat{W}^\alpha(s)$ and $\widehat{W}_{\Delta s}^\alpha(\mu)$ provides stable cosmological constraints that are robust to uncertainties in the halo–mass connection, thereby alleviating a key systematic challenge in galaxy survey analyses.

V. CONCLUSION

In this work, we developed a simulation-based inference framework to test the cosmological constraining power of MCFs. We used the KUN simulation suite as the training set and built a Gaussian Process emulator to predict MCF

statistics for different cosmological parameters. We then used the JUTIAN simulation to estimate the covariance matrix and to validate the emulator. Finally, we applied MCMC to mock data and constrained two cosmological parameters, Ω_m and σ_8 .

Our results show that MCFs can provide stronger cosmological constraints than 2PCF. This improvement is especially clear when several weighting exponents α are combined. For example, the joint use of $\alpha = [-0.5, -0.3, 0, 0.3, 0.5]$ gives a FoM about 2 times larger than that from the 2PCF alone. We also find that the two weighting choices, based on the local density ρ and the normalized density gradient $|\nabla\rho|/\rho$, contain complementary information. Their combination helps reduce parameter degeneracies and leads to tighter constraints.

We also studied how the results depend on scale selection. The constraining power of $\widehat{W}^\alpha(s)$ changes noticeably with the chosen range of s , showing that this statistic is sensitive to scale cuts. In comparison, the anisotropic statistic $\widehat{W}_{\Delta s}^\alpha(\mu)$ is less sensitive to the choice of maximum scale, although its constraining power still depends strongly on small-scale information.

An important result of this work is that the MCF constraints are stable under different halo selection choices. By changing the halo mass cut, we find that the constraints from $\widehat{W}^\alpha(s)$ and $\widehat{W}_{\Delta s}^\alpha(\mu)$ remain consistent and unbiased. This suggests that MCFs may be less sensitive to uncertainties in the galaxy–halo connection. Such robustness is important for future applications to observational galaxy surveys, where the relation between galaxies and dark matter halos is not perfectly known.

In summary, MCFs provide a useful extension of the standard 2PCF. By using environment-dependent weights such as ρ and $|\nabla\rho|/\rho$, and by combining multiple values of α , MCFs can extract additional non-Gaussian information from the cosmic density field. They improve cosmological parameter constraints and show good stability against changes in halo selection. These results suggest that MCFs are a promising and robust tool for cosmological analysis in next-generation galaxy surveys.

Acknowledgments

This work is supported by National SKA Program of China (2025SKA0160100), National Science Foundation of China (12473097), the China Manned Space Project with No. CMS-CSST-2021 (A02, A03, B01), Guangdong Basic and Applied Basic Research Foundation (2024A1515012309), the National Natural Science Foundation of China (12373005). We also acknowledge the Beijing Super Cloud Center (BSCC) and Beijing Beilong Super Cloud Computing Co., Ltd (<http://www.blsc.cn/>) for providing HPC resources that have significantly contributed to the research results presented in this paper.

[1] M. Colless, B. A. Peterson, C. Jackson, J. A. Peacock, S. Cole, P. Norberg, I. K. Baldry, C. M. Baugh, J. Bland-Hawthorn,

T. Bridges, et al., arXiv Astrophysics e-prints (2003), astro-

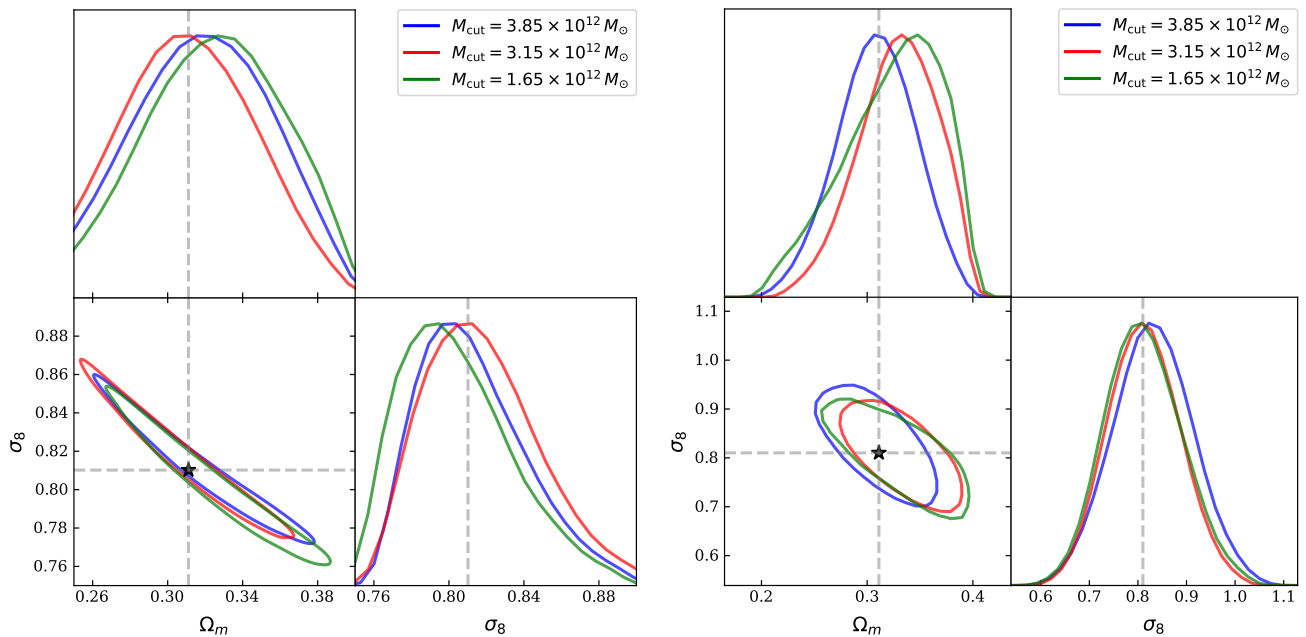


FIG. 13: Similar to Figure 7, but for different halo mass cuts $M_{\text{cut}} = 3.85, 3.15, \text{ and } 1.65 \times 10^{12} M_{\odot}$. The MCMC constraints for $\widehat{W}^{\alpha}(s)$ are shown in the left panel, and those for $\widehat{W}^{\alpha}(\mu)$ are shown in the right panel. In all cases, we adopt $\alpha = [-0.5, -0.3, 0, 0.3, 0.5]$ and the joint weighting scheme combining $w \propto \rho$ and $w \propto \nabla\rho/\rho$. The analysis is carried out using the fiducial binning scheme.

- ph/0306581.
- [2] F. Beutler, C. Blake, M. Colless, D. H. Jones, L. Staveley-Smith, G. B. Poole, L. Campbell, Q. Parker, W. Saunders, and F. Watson, *mnras* **423**, 3430 (2012), 1204.4725.
- [3] C. Blake, S. Brough, M. Colless, C. Contreras, W. Couch, S. Croom, T. Davis, M. J. Drinkwater, K. Forster, D. Gilbank, et al., *mnras* **415**, 2876 (2011), 1104.2948.
- [4] C. Blake, K. Glazebrook, T. M. Davis, S. Brough, M. Colless, C. Contreras, W. Couch, S. Croom, M. J. Drinkwater, K. Forster, et al., *mnras* **418**, 1725 (2011), 1108.2637.
- [5] D. G. York, J. Adelman, J. E. Anderson, Jr., S. F. Anderson, J. Annis, N. A. Bahcall, J. A. Bakken, R. Barkhouser, S. Bastian, E. Berman, et al., *aj* **120**, 1579 (2000), astro-ph/0006396.
- [6] D. J. Eisenstein, I. Zehavi, D. W. Hogg, R. Scoccimarro, M. R. Blanton, R. C. Nichol, R. Scranton, H.-J. Seo, M. Tegmark, Z. Zheng, et al., *Astrophys. J.* **633**, 560 (2005), astro-ph/0501171.
- [7] W. J. Percival, S. Cole, D. J. Eisenstein, R. C. Nichol, J. A. Peacock, A. C. Pope, and A. S. Szalay, *mnras* **381**, 1053 (2007), 0705.3323.
- [8] L. Anderson, E. Aubourg, S. Bailey, D. Bizyaev, M. Blanton, A. S. Bolton, J. Brinkmann, J. R. Brownstein, A. Burden, A. J. Cuesta, et al., *mnras* **427**, 3435 (2012), 1203.6594.
- [9] S. Alam, M. Ata, S. Bailey, F. Beutler, D. Bizyaev, J. A. Blazek, A. S. Bolton, J. R. Brownstein, A. Burden, C.-H. Chuang, et al., *mnras* **470**, 2617 (2017), 1607.03155.
- [10] N. Kaiser, *Monthly Notices of the Royal Astronomical Society* **227**, 1 (1987).
- [11] W. E. Ballinger, J. A. Peacock, and A. F. Heavens, *Monthly Notices of the Royal Astronomical Society* **282**, 877 (1996), astro-ph/9605017.
- [12] D. J. Eisenstein and W. Hu, *The Astrophysical Journal* **496**, 605 (1998), astro-ph/9709112.
- [13] C. Blake and K. Glazebrook, *The Astrophysical Journal* **594**, 665 (2003), astro-ph/0301632.
- [14] H.-J. Seo and D. J. Eisenstein, *The Astrophysical Journal* **598**, 720 (2003), astro-ph/0307460.
- [15] M. Colless, B. A. Peterson, C. Jackson, J. A. Peacock, S. Cole, P. Norberg, I. K. Baldry, C. M. Baugh, J. Bland-Hawthorn, T. Bridges, et al., arXiv e-prints astro-ph/0306581 (2003), astro-ph/0306581.
- [16] F. Beutler, C. Blake, M. Colless, D. H. Jones, L. Staveley-Smith, G. B. Poole, L. Campbell, Q. Parker, W. Saunders, and F. Watson, *Monthly Notices of the Royal Astronomical Society* **423**, 3430 (2012), ISSN 0035-8711, <https://academic.oup.com/mnras/article-pdf/423/4/3430/4903419/mnras0423-3430.pdf>, URL <https://doi.org/10.1111/j.1365-2966.2012.21136.x>.
- [17] C. Blake, K. Glazebrook, T. M. Davis, S. Brough, M. Colless, C. Contreras, W. Couch, S. Croom, M. J. Drinkwater, K. Forster, et al., *Monthly Notices of the Royal Astronomical Society* **418**, 1725 (2011), 1108.2637.
- [18] C. Blake, S. Brough, M. Colless, C. Contreras, W. Couch, S. Croom, T. Davis, M. J. Drinkwater, K. Forster, D. Gilbank, et al., *Monthly Notices of the Royal Astronomical Society* **415**, 2876 (2011), 1104.2948.
- [19] D. G. York, J. Adelman, J. Anderson, John E., S. F. Anderson, J. Annis, N. A. Bahcall, J. A. Bakken, R. Barkhouser, S. Bastian, E. Berman, et al., *The Astronomical Journal* **120**, 1579 (2000), astro-ph/0006396.
- [20] A. G. Sánchez, C. G. Scóccola, A. J. Ross, W. Percival, M. Manera, F. Montesano, X. Mazzalay, A. J. Cuesta, D. J. Eisenstein, E. Kazin, et al., *Monthly Notices of the Royal Astronomical Society* **425**, 415 (2012), 1203.6616.
- [21] A. G. Sánchez, E. A. Kazin, F. Beutler, C.-H. Chuang, A. J. Cuesta, D. J. Eisenstein, M. Manera, F. Montesano, R. C. Nichol, N. Padmanabhan, et al., *Monthly Notices of the Royal Astronomical Society* **433**, 1202 (2013), 1303.4396.

- [22] L. Anderson, É. Aubourg, S. Bailey, F. Beutler, V. Bhardwaj, M. Blanton, A. S. Bolton, J. Brinkmann, J. R. Brownstein, A. Burden, et al., *Monthly Notices of the Royal Astronomical Society* **441**, 24 (2014), 1312.4877.
- [23] L. Samushia, B. A. Reid, M. White, W. J. Percival, A. J. Cuesta, G.-B. Zhao, A. J. Ross, M. Manera, É. Aubourg, F. Beutler, et al., *Monthly Notices of the Royal Astronomical Society* **439**, 3504 (2014), 1312.4899.
- [24] A. J. Ross, L. Samushia, C. Howlett, W. J. Percival, A. Burden, and M. Manera, *Monthly Notices of the Royal Astronomical Society* **449**, 835 (2015), 1409.3242.
- [25] F. Beutler, H.-J. Seo, A. J. Ross, P. McDonald, S. Saito, A. S. Bolton, J. R. Brownstein, C.-H. Chuang, A. J. Cuesta, D. J. Eisenstein, et al., *Monthly Notices of the Royal Astronomical Society* **464**, 3409 (2017), 1607.03149.
- [26] A. G. Sánchez, J. N. Grieb, S. Salazar-Albornoz, S. Alam, F. Beutler, A. J. Ross, J. R. Brownstein, C.-H. Chuang, A. J. Cuesta, D. J. Eisenstein, et al., *Monthly Notices of the Royal Astronomical Society* **464**, 1493 (2017), 1607.03146.
- [27] C.-H. Chuang, F.-S. Kitaura, Y. Liang, A. Font-Ribera, C. Zhao, P. McDonald, and C. Tao, *Physical Review D* **95**, 063528 (2017), 1605.05352.
- [28] DESI Collaboration, A. Aghamousa, J. Aguilar, S. Ahlen, S. Alam, L. E. Allen, C. Allende Prieto, J. Annis, S. Bailey, C. Balland, et al., arXiv e-prints arXiv:1611.00036 (2016), 1611.00036.
- [29] LSST Science Collaboration, P. A. Abell, J. Allison, S. F. Anderson, J. R. Andrew, J. R. P. Angel, L. Armus, D. Arnett, S. J. Asztalos, T. S. Axelrod, et al., arXiv e-prints arXiv:0912.0201 (2009), 0912.0201.
- [30] R. Laureijs, J. Amiaux, S. Arduini, J. L. Auguères, J. Brinchmann, R. Cole, M. Cropper, C. Dabin, L. Duvet, A. Ealet, et al., arXiv e-prints arXiv:1110.3193 (2011), 1110.3193.
- [31] Euclid Collaboration, Y. Mellier, Abdurro'uf, J. A. Acevedo Barroso, A. Achúcarro, J. Adamek, R. Adam, G. E. Addison, N. Aghanim, M. Agüena, et al., arXiv e-prints arXiv:2405.13491 (2024), 2405.13491.
- [32] O. Dore, C. Hirata, Y. Wang, D. Weinberg, T. Eifler, R. J. Foley, C. H. Heinrich, E. Krause, S. Perlmutter, A. Pisani, et al., *Bull. Amer. Astron. Soc.* **51**, 341 (2019), 1904.01174.
- [33] Y. Gong, X. Liu, Y. Cao, X. Chen, Z. Fan, R. Li, X.-D. Li, Z. Li, X. Zhang, and H. Zhan, *Astrophys. J.* **883**, 203 (2019), 1901.04634.
- [34] C. G. Sabiu, D. F. Mota, C. Llinares, and C. Park, *Astronomy and Astrophysics* **592**, A38 (2016), 1603.05750.
- [35] Z. Slepian, D. J. Eisenstein, J. R. Brownstein, C.-H. Chuang, H. Gil-Marín, S. Ho, F.-S. Kitaura, W. J. Percival, A. J. Ross, G. Rossi, et al., *Monthly Notices of the Royal Astronomical Society* **469**, 1738 (2017), 1607.06097.
- [36] C. G. Sabiu, B. Hoyle, J. Kim, and X.-D. Li, *The Astrophysical Journals* **242**, 29 (2019), 1901.00296.
- [37] B. S. Ryden, *The Astrophysical Journal* **452**, 25 (1995), astro-ph/9506028.
- [38] G. Lavaux and B. D. Wandelt, *The Astrophysical Journal* **754**, 109 (2012), 1110.0345.
- [39] S. Ravanbakhsh, J. Oliva, S. Fromenteau, L. C. Price, S. Ho, J. Schneider, and B. Poczós, arXiv e-prints (2017), 1711.02033.
- [40] A. Mathuriya, D. Bard, P. Mendygral, L. Meadows, J. Arneemann, L. Shao, S. He, T. Karna, D. Moise, S. J. Pennycook, et al., arXiv e-prints (2018), 1808.04728.
- [41] S. Pan, M. Liu, J. Forero-Romero, C. G. Sabiu, Z. Li, H. Miao, and X.-D. Li, *Science China Physics, Mechanics & Astronomy* **63**, 110412 (2020).
- [42] C. Beisbart and M. Kerscher, *The Astrophysical Journal* **545**, 6 (2000), astro-ph/0003358.
- [43] C. Beisbart, M. Kerscher, and K. Mecke (2002), vol. 600, pp. 358–390.
- [44] S. Gottlöber, M. Kerscher, A. V. Kravtsov, A. Faltenbacher, A. Klypin, and V. Müller, *Astronomy and Astrophysics* **387**, 778 (2002), astro-ph/0203148.
- [45] R. K. Sheth and G. Tormen, *Monthly Notices of the Royal Astronomical Society* **350**, 1385 (2004), astro-ph/0402237.
- [46] R. K. Sheth, A. J. Connolly, and R. Skibba (2005), astro-ph/0511773.
- [47] R. Skibba, R. K. Sheth, A. J. Connolly, and R. Scranton, *Monthly Notices of the Royal Astronomical Society* **369**, 68 (2006), astro-ph/0512463.
- [48] M. White and N. Padmanabhan, *Monthly Notices of the Royal Astronomical Society* **395**, 2381 (2009), 0812.4288.
- [49] M. White, *JCAP* **2016**, 057 (2016), 1609.08632.
- [50] S. Satpathy, R. A C Croft, S. Ho, and B. Li, *Monthly Notices of the Royal Astronomical Society* **484**, 2148 (2019), 1901.01447.
- [51] E. Massara, F. Villaescusa-Navarro, S. Ho, N. Dalal, and D. N. Spergel, *Physical Review Letters* **126**, 011301 (2021).
- [52] O. H. E. Philcox, E. Massara, and D. N. Spergel (2020), 2006.10055.
- [53] Y. Yang, H. Miao, Q. Ma, M. Liu, C. G. Sabiu, J. Forero-Romero, Y. Huang, L. Lai, Q. Qian, Y. Zheng, et al., *The Astrophysical Journal* **900**, 6 (2020).
- [54] X. Xiao, Y. Yang, X. Luo, J. Ding, Z. Huang, X. Wang, Y. Zheng, C. G. Sabiu, J. Forero-Romero, H. Miao, et al., *Monthly Notices of the Royal Astronomical Society* **513**, 595–603 (2022), ISSN 1365-2966, URL <http://dx.doi.org/10.1093/mnras/stac879>.
- [55] L. Lai, J. Ding, X. Luo, Y. Yang, Z. Wang, K. Liu, G. Liu, X. Wang, Y. Zheng, Z. Li, et al., *Science China Physics, Mechanics & Astronomy* **67** (2024), ISSN 1869-1927, URL <http://dx.doi.org/10.1007/s11433-023-2384-4>.
- [56] K. Heitmann, D. Higdon, M. White, S. Habib, B. J. Williams, E. Lawrence, and C. Wagner, *Astrophys. J.* **705**, 156 (2009), 0902.0429.
- [57] K. Heitmann, M. White, C. Wagner, S. Habib, and D. Higdon, *Astrophys. J.* **715**, 104 (2010), 0812.1052.
- [58] E. Lawrence, K. Heitmann, M. White, D. Higdon, C. Wagner, S. Habib, and B. Williams, *Astrophys. J.* **713**, 1322 (2010), 0912.4490.
- [59] K. Heitmann, E. Lawrence, J. Kwan, S. Habib, and D. Higdon, *Astrophys. J.* **780**, 111 (2014), 1304.7849.
- [60] E. Lawrence, K. Heitmann, J. Kwan, A. Upadhye, D. Bingham, S. Habib, D. Higdon, A. Pope, H. Finkel, and N. Frontiere, *Astrophys. J.* **847**, 50 (2017), 1705.03388.
- [61] S. Bocquet, K. Heitmann, S. Habib, E. Lawrence, T. Uram, N. Frontiere, A. Pope, and H. Finkel, arXiv e-prints (2020), 2003.12116.
- [62] J. Kwan, K. Heitmann, S. Habib, N. Padmanabhan, E. Lawrence, H. Finkel, N. Frontiere, and A. Pope, *The Astrophysical Journal* **810**, 35 (2015).
- [63] B. D. Wibking, D. H. Weinberg, A. N. Salcedo, H.-Y. Wu, S. Singh, S. Rodríguez-Torres, L. H. Garrison, and D. J. Eisenstein, *Monthly Notices of the Royal Astronomical Society* **492**, 2872–2896 (2019), ISSN 1365-2966, URL <http://dx.doi.org/10.1093/mnras/stz3423>.
- [64] J. Kwan, S. Bhattacharya, K. Heitmann, and S. Habib, *The Astrophysical Journal* **768**, 123 (2013), ISSN 1538-4357, URL <http://dx.doi.org/10.1088/0004-637X/768/2/123>.
- [65] T. Nishimichi et al., *The Astrophysical Journal* **884**, 29 (2019), ISSN 1538-4357, URL <http://dx.doi.org/10.3847/1538-4357/ab3719>.

- [66] Y. Kobayashi, T. Nishimichi, M. Takada, R. Takahashi, and K. Osato, arXiv e-prints arXiv:2005.06122 (2020), 2005.06122.
- [67] J. Kwan, S. Saito, A. Leauthaud, K. Heitmann, S. Habib, N. Frontiere, H. Guo, S. Huang, A. Pope, and S. Rodríguez-Torres, *Astrophys. J.* **952**, 80 (2023), 2302.12379.
- [68] K. R. Moran, K. Heitmann, E. Lawrence, S. Habib, D. Bingham, A. Upadhye, J. Kwan, D. Higdon, and R. Payne, *Mon. Not. R. Astron. Soc.* **520**, 3443 (2023), 2207.12345.
- [69] K. Cranmer, J. Brehmer, and G. Louppe, *Proceedings of the National Academy of Sciences* **117**, 30055–30062 (2020), ISSN 1091-6490, URL <http://dx.doi.org/10.1073/pnas.1912789117>.
- [70] Z. Chen, Y. Yu, J. Han, and Y. P. Jing, arXiv e-prints arXiv:2502.11160 (2025), 2502.11160.
- [71] V. Springel, R. Pakmor, O. Zier, and M. Reinecke, *Monthly Notices of the Royal Astronomical Society* **506**, 2871–2949 (2021), ISSN 1365-2966, URL <http://dx.doi.org/10.1093/mnras/stab1855>.
- [72] J. Han, M. Li, W. Jiang, Z. Chen, H. Wang, C. Wei, F. He, J. He, J. Zhang, Y. Liu, et al., *The jiu Tian simulations for the csst extra-galactic surveys* (2025), 2503.21368, URL <https://arxiv.org/abs/2503.21368>.
- [73] I. Sobol, *Vychisl. Mat. i Mater. Phys* **7**, 784 (1967).
- [74] Planck Collaboration, N. Aghanim, Y. Akrami, M. Ashdown, J. Aumont, C. Baccigalupi, M. Ballardini, A. J. Banday, R. B. Barreiro, N. Bartolo, et al., *Astron. Astrophys.* **641**, A6 (2020), 1807.06209.
- [75] R. E. Angulo and A. Pontzen, *Mon. Not. R. Astron. Soc.* **462**, L1 (2016), 1603.05253.
- [76] P. S. Behroozi, R. H. Wechsler, and H.-Y. Wu, *The Astrophysical Journal* **762**, 109 (2012), ISSN 1538-4357, URL <http://dx.doi.org/10.1088/0004-637X/762/2/109>.
- [77] M. Davis, G. Efstathiou, C. S. Frenk, and S. D. M. White, *Astrophys. J.* **292**, 371 (1985).
- [78] V. Springel, S. D. M. White, G. Tormen, and G. Kauffmann, *Monthly Notices of the Royal Astronomical Society* **328**, 726–750 (2001), ISSN 1365-2966, URL <http://dx.doi.org/10.1046/j.1365-8711.2001.04912.x>.
- [79] L. B. Lucy, *Astron. J.* **82**, 1013 (1977).
- [80] R. A. Gingold and J. J. Monaghan, *Monthly Notices of the Royal Astronomical Society* **181**, 375 (1977), ISSN 0035-8711, <https://academic.oup.com/mnras/article-pdf/181/3/375/3104055/mnras181-0375.pdf>, URL <https://doi.org/10.1093/mnras/181.3.375>.
- [81] C. K. Williams and C. E. Rasmussen, *Gaussian processes for machine learning*, vol. 2 (MIT press, Cambridge, MA., 2006), 3rd ed.
- [82] H. Zhang, Y.-C. Wang, T.-J. Zhang, and T. Zhang, *The Astrophysical Journal Supplement Series* **266**, 27 (2023), ISSN 1538-4365, URL <http://dx.doi.org/10.3847/1538-4365/accb92>.
- [83] F. Pedregosa, G. Varoquaux, A. Gramfort, V. Michel, B. Thirion, O. Grisel, M. Blondel, P. Prettenhofer, R. Weiss, V. Dubourg, et al., *Journal of Machine Learning Research* **12**, 2825 (2011).
- [84] S. Yuan, L. H. Garrison, D. J. Eisenstein, and R. H. Wechsler, *Monthly Notices of the Royal Astronomical Society* **515**, 871–896 (2022), ISSN 1365-2966, URL <http://dx.doi.org/10.1093/mnras/stac1830>.
- [85] J. Hartlap, P. Simon, and P. Schneider, *Astronomy & Astrophysics* **464**, 399–404 (2006), ISSN 1432-0746, URL <http://dx.doi.org/10.1051/0004-6361:20066170>.
- [86] D. Foreman-Mackey, D. W. Hogg, D. Lang, and J. Goodman, *PASP* **125**, 306 (2013), 1202.3665.
- [87] A. Lewis, *Journal of Cosmology and Astroparticle Physics* **2025**, 025 (2025), ISSN 1475-7516, URL <http://dx.doi.org/10.1088/1475-7516/2025/08/025>.
- [88] Y. Wang, *Phys. Rev. D* **77**, 123525 (2008), URL <https://link.aps.org/doi/10.1103/PhysRevD.77.123525>.